



# Optics Letters

## Edge sparsity criterion for robust holographic autofocusing

YIBO ZHANG,<sup>1,2,3</sup>  HONGDA WANG,<sup>1,2,3</sup>  YICHEN WU,<sup>1,2,3</sup> MIU TAMAMITSU,<sup>1,2,3</sup> AND AYDOGAN OZCAN<sup>1,2,3,4,\*</sup> 

<sup>1</sup>Electrical Engineering Department, University of California, Los Angeles, California 90095, USA

<sup>2</sup>Bioengineering Department, University of California, Los Angeles, California 90095, USA

<sup>3</sup>California NanoSystems Institute (CNSI), University of California, Los Angeles, California 90095, USA

<sup>4</sup>Department of Surgery, David Geffen School of Medicine, University of California, Los Angeles, California 90095, USA

\*Corresponding author: ozcan@ucla.edu

Received 10 July 2017; revised 29 August 2017; accepted 30 August 2017; posted 31 August 2017 (Doc. ID 302019); published 22 September 2017

**Autofocusing is essential to digital holographic imaging. Previously used autofocusing criteria exhibit challenges when applied to, e.g., connected objects with different optical properties. Furthermore, in some of the earlier autofocusing criteria, the polarity, i.e., whether to search for the peak or the valley as a function of depth, changes for different types of samples, which creates another challenge. Here, we propose a robust and accurate autofocusing criterion that is based on the edge sparsity of the complex optical wavefront, which we termed the “sparsity of the gradient” (SoG). We demonstrated the success of SoG by imaging a wide range of objects, including resolution test targets, stained and unstained Papanicolaou smears, stained tissue sections, and blood smears.** © 2017 Optical Society of America

**OCIS codes:** (090.1995) Digital holography; (110.0180) Microscopy; (090.2880) Holographic interferometry; (100.2960) Image analysis.

<https://doi.org/10.1364/OL.42.003824>

Digital holography [1] enables computational refocusing within a 3D sample volume after the image acquisition. This unique advantage has made it a useful technique in various applications such as bio-fluid analysis [2], dynamic 3D tracking of sperms [3], monitoring of living cells [4], among many others. Recently, it was also shown that digital holography in a lensless in-line format can achieve high-throughput imaging of tissue slides and cell smears on a chip [5,6].

Digital refocusing and reconstruction of holograms rely on the precise knowledge of the defocus distance (i.e., the “z distance”) of the object of interest. A widely accepted autofocusing method involves digital refocusing of a hologram using various  $z$  distances, where a certain function, i.e., an autofocusing criterion, is evaluated based on this set of refocused images. The  $z$  distance that corresponds to the maximum (or sometimes the minimum) of this criterion is used as the focus distance of the object for that given hologram. A good autofocusing criterion should in general be unimodal over a wide range of  $z$  distances and be accurate for various types of samples [7].

Numerous autofocusing criteria have been demonstrated for different holographic imaging applications and were successfully used to image various samples [4,8–14]. For example, Gillespie and King proposed to use self-entropy (SEN) as an autofocusing criterion in digital holography and successfully applied it to test images [8]. As an alternative, Liebling and Unser used the sparsity of the Fresnel coefficients (FRES) as an autofocusing criterion and applied it for imaging resolution test targets [9]. Dubois *et al.* used the integrated amplitude (AMP) as an autofocusing criterion for pure amplitude and pure phase objects, with opposite polarities [10]. Later a modified version of AMP was also proposed using integrated high-pass-filtered amplitude (HPA), which was demonstrated to lead to a minimum for both amplitude and phase objects [11]. Langehanenberg *et al.* compared four different autofocusing criteria for imaging of pure-phase objects, including the summed weighted power spectrum (SPEC), variance (VAR), summed gradient (GRA), and summed Laplacian (LAP) to validate the applicability of SPEC and GRA on pure-phase objects [4]. Memmolo *et al.* proposed to use the contrast texture measure (i.e., the Tamura coefficient, TC) as an autofocusing criterion and demonstrated successful results based on off-axis holography using macroscopic objects [12]. Later, Memmolo *et al.* also used a sparsity measure, i.e., the Gini index (GI), as an autofocusing criterion to image microscopic objects, e.g., cells [13]. Recently, Lyu *et al.* used the axial magnitude differential (DIF) as another autofocusing criterion and discussed its applicability to amplitude-contrast and phase-contrast samples [14].

Despite the wide variety of available autofocusing criteria, the choice of the specific criterion is, unfortunately, still highly *subjective* depending on the object type or application of interest. Development of a robust and accurate autofocusing criterion for digital holography that works universally well for different types of samples is a challenging task for several reasons. First, the coherent diffraction of light in holography results in complex interference patterns, in addition to speckle- and multiple-reflection-related interference artifacts, instead of providing homogeneous smoothing as in the case of incoherent microscopy and photography. Therefore, the sharpness or the high-frequency spatial content of a holographic image does not necessarily diminish with defocusing. Moreover, without

phase retrieval, the twin image artifact in in-line holography makes autofocusing more challenging. These explain some of the failures of directly applying autofocusing criteria developed for incoherent imaging to holography. Second, different mechanisms of light–matter interaction result in different complex-valued transmission functions corresponding to the samples. For example, a phase object, such as a transparent and unlabeled cell, interacts with the illumination light mainly through perturbations to the optical phase of the transmitted wavefront, leaving its amplitude mostly unchanged. On the other hand, an amplitude object, such as a metal-coated resolution test target, mainly modulates the amplitude of the transmitted wave, whereas a *stained* cell or tissue section that is semitransparent would both modulate the phase and amplitude. These variations among different types of objects make some of the autofocusing criteria that are based on, e.g., the sharpness of the features, contrast, sparsity or other properties of the amplitude channel of the complex field, less robust. Furthermore, many of these criteria change polarity for amplitude-contrast versus phase-contrast samples and fail or perform suboptimal for mixed amplitude- and phase-contrast samples [10,14]. Some of the previous work also explored applying a criterion on the phase channel of the complex field for autofocusing [8], but these approaches suffer from the same limitations discussed earlier, besides facing phase-wrapping-related challenges.

Here we propose a robust autofocusing criterion for digital holography that performs accurate depth focusing across a wide range of samples, including amplitude-only, phase-only, and mixed-object types. We termed this criterion “sparsity of the gradient” (SoG), which is based on the *edge sparsity* of an object’s in-focus image. SoG of a complex optical wavefront  $U$  is defined as

$$\text{SoG}(U) = S(|\nabla U|), \quad (1)$$

where  $\nabla$  is the gradient operator,  $|\cdot|$  is the modulus operator, and  $S(\cdot)$  is a sparsity measure.  $|\nabla U|$  can be calculated for a complex-valued image as  $|\nabla U|_{ij}^2 = |U_{ij} - U_{i,j-1}|^2 + |U_{ij} - U_{i-1,j}|^2$ .

Under the SoG framework, we used two different sparsity measures, GI and TC, which we term “Gini of the gradient” (GoG) and “Tamura of the gradient” (ToG), respectively. One should note that TC has recently been proven to be a sparsity measure [15]. These two sparsity measures (GI and TC) were chosen to quantify the edge sparsity of a complex image because they exhibit advantages, such as invariance under scaling, compared with other sparsity measures [15,16].

GI is defined for a real and non-negative image ( $C$ ) as

$$\text{GI}(C) = 1 - 2 \sum_{k=1}^N \frac{a_{[k]}}{\text{sum}(C)} \left( \frac{N - k + 0.5}{N} \right), \quad (2)$$

where  $a_{[k]}$  is the  $k$ -th sorted entry of the image matrix,  $C$ , in ascending order,  $k = 1, \dots, N$ , and  $\text{sum}(C)$  is the sum of all the entries of the image. TC is defined as

$$\text{TC}(C) = \sqrt{\sigma(C)/\langle C \rangle}, \quad (3)$$

where  $\sigma(\cdot)$  is the standard deviation, and  $\langle \cdot \rangle$  is the mean.

The design of the SoG criterion for autofocusing assumes that the images of natural objects are mostly composed of flat regions and sharp edges, which is a widely accepted assumption utilized in image compression, image denoising, etc. When a refocused complex optical wavefront corresponding to a physical object is *in focus*, sharp edges should be sparse, i.e., the sharpest transitions in the image should only take up a small fraction of the image’s total area.

As opposed to most of the other autofocusing criteria that operate on the amplitude channel of a refocused image, SoG operates directly on the *complex* refocused image, which makes it much more general and robust for amplitude contrast, phase contrast, or mixed object types. The gradient operator in the definition of SoG can sense the sharp changes in an image regardless of the specific amplitude and/or phase-contrast mechanism of the object of interest. As a consequence, SoG is expected to always reach its *maximum* at the correct focus distance regardless of the type of the object, which is another advantage over some of the previously reported autofocusing criteria, which usually exhibit opposite polarity for amplitude- versus phase-contrast objects and an ambiguous polarity for mixed amplitude/phase-contrast objects.

To compare the performance of GoG and ToG against the state-of-the-art, we selected eight previously proposed autofocusing criteria, including SEN, FRES, HPA, SPEC, GRA, TC, GI, and DIF. Note that VAR and LAP [4] criteria are analogous to TC and GRA [4,12], respectively; therefore, they were not duplicated in our comparison. We used five different types of quasi-planar samples to validate our method, including a USAF resolution test target, an unstained Pap smear, a stained Pap smear (Pap stain, ThinPrep preparation), a 4  $\mu\text{m}$  thick H&E-stained lung tissue section, and a Wright-stained whole blood smear. Among these objects, the USAF test target can be considered as an amplitude-contrast object, the unstained Pap smear can be considered as a phase-contrast object, while the others can be considered as mixed amplitude- and phase-contrast objects. We validated that both GoG and ToG outperform the existing autofocusing criteria, providing superior accuracy and robustness for different types of amplitude-contrast, phase-contrast, and mixed amplitude- and phase-contrast objects.

Moreover, all the digital autofocusing experiments reported here were performed without any phase-retrieval using in-line holograms of spatially connected samples that violate the “weakly scattering” condition; stated differently, the refocused images were severely contaminated by the twin image artifact, making autofocusing much more challenging. This demonstrates that GoG and ToG are robust and accurate even under noisy conditions and also illustrates their practical usefulness for in-line holography, where the knowledge of the  $z$  distances is usually a prerequisite for the subsequent phase retrieval step; therefore, autofocusing on the non-phase-retrieved hologram is usually an inevitable initial step for image reconstruction [5,6]. We also tested GoG and ToG on various phase-retrieved holograms, where they also performed very well [15]. Therefore, we believe GoG and ToG (or SoG in general) also can be applied to off-axis holographic imaging.

The raw holograms corresponding to the test objects were captured using a lens-free in-line holography setup, with pixel super-resolution implemented on a chip [5], achieving an effective pixel size of  $\sim 0.37 \mu\text{m}$  at both the hologram and object reconstruction planes. To create the “ground truth” focus distance for each sample, we took the following two steps: first, multiheight phase retrieval [5] using eight hologram heights was performed using manually found *relative*  $z$  distances with respect to the first hologram height. The relative  $z$  distances were found such that their refocused images looked most alike. Second, we used the *phase-retrieved complex-valued hologram* at the plane closest to the sample to perform manual refocusing to create the ground truth *absolute* focus distance based on visual

judgment. We used  $z$  increments of  $\sim 1 \mu\text{m}$ , as any change in  $z$  below  $1 \mu\text{m}$  is hardly noticeable to the human eye for this imaging system.

For each autofocus criterion we used in our comparison, in order to rapidly find the resulting focus distance, to be compared with the ground truth focus distance discussed earlier, we custom-wrote a search algorithm based on the golden-section search method [17], composed of five steps: (1) Using the selected autofocus criterion, conduct a rough scan between  $z = 100 \mu\text{m}$  and  $z = 800 \mu\text{m}$  with a step size of  $10 \mu\text{m}$ ;  $z = 0 \mu\text{m}$  defines the plane of the imager chip. (2) Define a  $40 \mu\text{m}$  search range around the maximum (or minimum, depending on the selected criterion) of the rough scan in (1). (3) Evaluate the focus criterion at  $4M + 1$  equally spaced  $z$  distances spanning the search range defined in (2); identify the maximum (or minimum) of the search (we used  $M = 3$ ). (4) Check unimodality based on these  $4M + 1$  points; if not unimodal, shrink the search range in half around the maximum (or minimum) point, where  $2M$  new points need to be evaluated; repeat until unimodality is reached. (5) After unimodality is confirmed, conduct an iterative golden-section search within the search range to identify the maximum (or minimum). The search stops when the search range is  $< 0.01 \mu\text{m}$ .

Based on this evaluation process, the autofocus accuracies of 10 different criteria (GoG, ToG, HPA, GRA, SEN, GI, SPEC, DIF, TC, and FRES) were compared with the gold standard focus distances for different objects (Table 1). To overcome the ambiguity of polarity based on the sample type, we automatically searched for both the peaks (“max”) and valleys (“min”) for all the criteria, except for GoG, ToG, and FRES (only max) and HPA (only min). To better visualize the results, we color-coded Table 1 with a color map, representing the errors made in focus distances, ranging from 0 and  $10 \mu\text{m}$ . In the same table,  $> 10 \mu\text{m}$  errors are colored as gray, considered as “failure.” “NaN” represents a case where max/min criterion is found at the boundary of the search range. Evidently, GoG and ToG performed very well for all the sample types. Their largest errors ( $1.66 \mu\text{m}$  and  $1.52 \mu\text{m}$ , respectively) occurred for the stained Pap smear, which are comparable to the  $1 \mu\text{m}$  uncertainty resulting from human error in manual focusing.

For the other autofocus criteria, first let us focus on their performance on the USAF test target (an amplitude-contrast object) and the unstained Pap smear (a phase-contrast object). If we consider the smaller error of the two polarities (max versus

min) wherever applicable, HPA, GRA, GI, and TC had errors less than or around  $1 \mu\text{m}$ . We also observed polarity inversion for GRA, GI, and TC when switched from the USAF test target to an unstained Pap smear sample, which also has been reported in the literature [13,14]. The other criteria, SEN, SPEC, DIF, and FRES, failed for at least one of the two samples (Table 1). As for the performance of these autofocus criteria for the other three samples, including the stained Pap smear, lung tissue and blood smear samples, we see that HPA, SEN, GI, SPEC, DIF, TC, and FRES each failed for at least one sample. GRA had  $> 2 \mu\text{m}$  but  $< 4 \mu\text{m}$  errors for all three samples, but the polarity changed among the objects, which might be due to the relative extent of amplitude-contrast and phase-contrast of each sample.

To gain more insight into the behavior of different autofocus criteria, we took the stained Pap smear sample as an example and plotted the values of each criterion against  $z$ , as shown in Fig. 1. The SPEC, SEN, and DIF exhibit significant oscillations, which make it difficult to search for a peak or valley. GI and TC do not have a peak/valley at the actual  $z$ , but they both have a large slope around it. GRA has a peak and a valley on the opposite sides of the correct  $z$  value, and the curve is also slightly fuzzy. FRES and HPA each have a peak/valley

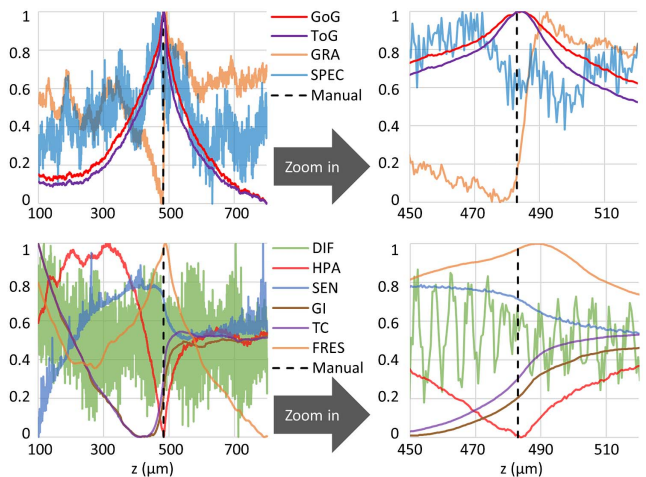


**Fig. 1.** Different autofocus criteria as a function of  $z$ , using a stained Pap smear sample. To ensure the visibility of the curves, the criteria were divided in two parts (upper and lower panels). Dashed line shows correct  $z$  distance.

**Table 1. Absolute Errors (in  $\mu\text{m}$ ) of Various Autofocusing Criteria on Different Samples<sup>a</sup>**

Method	GoG	ToG	HPA	GRA	SEN	GI	SPEC	DIF	TC	FRES	Color scale						
Polarity	Max	Max	Min	Min	Max	Min	Max	Min	Max	Min	Max						
USAF target	0.96	1.02	1.11	494.1	0.07	0.84	505.2	NaN	0.34	518.1	12.52	NaN	179.6	NaN	0.18	1.33	$> 10 \mu\text{m}$ and NaN
Unstained Pap smear	0.10	0.04	0.98	0.06	104.3	10.54	436.0	0.70	NaN	0.00	148.5	127.0	0.06	0.93	NaN	NaN	
Stained Pap smear	1.66	1.52	0.75	3.14	9.27	NaN	79.00	68.66	NaN	130.9	12.32	227.4	353.9	71.52	NaN	6.28	$10 \mu\text{m}$
Lung tissue	0.12	0.54	NaN	2.35	6.97	16.46	296.1	17.59	NaN	NaN	6.93	19.90	334.4	18.64	NaN	4.09	
Blood smear	1.08	1.10	19.78	4.38	2.90	5.21	81.77	41.02	7.14	NaN	0.89	2.23	282.1	41.00	7.85	NaN	0

<sup>a</sup>For all criteria except GoG, ToG, HPA, and FRES, both minimum and maximum were searched.

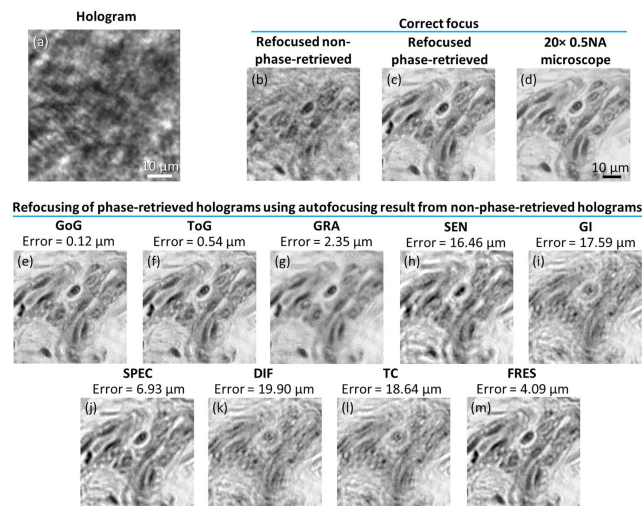
near the correct  $z$  but are not unimodal. GoG and ToG, on the other hand, are overall smooth, unimodal, and each has a strong global peak close to the correct  $z$  value, as desired.

Figure 2 further provides a comparison of the refocusing results based on our criteria. To enable better visual judgment, the phase-retrieved hologram of a lung tissue sample using eight sample heights was refocused, where each focus distance was estimated from the non-phase-retrieved hologram. Figures 2(e)–2(m) clearly shows that GoG and ToG provide the best in-focus images, which contain sharp features of the cells and the tissue morphology that agree well with a  $20 \times 0.5$  NA microscope objective image.

Summarizing this comparison, all the criteria other than GoG, ToG, and GRA failed for at least one sample. The average errors for GoG, ToG, and GRA for all the samples were 0.78, 0.84, and  $1.70 \mu\text{m}$ , respectively, where the smaller errors between min and max were considered for quantification of the error in GRA (to its advantage). Polarity inversion was observed among different sample types as a disadvantage of GRA, which may cause confusion when autofocusing an unknown sample. An additional challenge with any autofocusing criterion that has polarity inversion is that there can be a particular specimen that has a certain level of amplitude and phase contrast such that it is exactly at (or close to) the point of polarity inversion, which can create a singularity point and the correct  $z$  cannot be determined.

Although GoG and ToG performed similarly for dense objects, we also noticed that, for naturally sparse samples of small size, such as dilute *Giardia lamblia* cysts and sperm cells, the user sometimes needs to choose a region of interest that tightly bounds the object of interest when using GoG. This constraint is relaxed when using ToG, leading to more flexibility. Mathematical origins of this different behavior of GoG and ToG for naturally sparse samples are discussed in detail in [15].

In addition to the autofocus criteria discussed thus far, we also tested the recently proposed complex ratio [18], which failed for some of the samples. We also tried cascading existing criteria onto the gradient of the complex refocused image, creating



**Fig. 2.** Comparison of the autofocusing accuracy of different criteria using a lung tissue sample. (a) Hologram intensity. (b)–(d) Holographic and  $20 \times 0.5$  NA microscope images at the correct focus. (e)–(m) Refocused image amplitude using all the autofocusing criteria except HPA, which failed to find a minimum. The smaller autofocusing error between the min and max is displayed, wherever applicable.

**Table 2. Comparison of Computation Times**

Method	GoG	ToG	HPA	GRA	SEN	GI	SPEC	DIF	TC	FRES
Time (ms)	177	134	106	97	170	142	109	190	114	392

various new criteria such as AMP of the gradient, SEN of the gradient, SPEC of the gradient, etc. These also failed for some of the samples and therefore were not included in our comparison.

Computational efficiency is another important feature of an autofocus criterion that needs to be considered. We performed a comparison of the run times of different autofocusing criteria using a laptop computer equipped with an Intel Core i7-7700HQ CPU at 2.80 GHz and 16 GB of memory; GPU acceleration was not used. The total time required to refocus a hologram of  $1024 \times 1024$  pixels and evaluate each autofocusing criterion is summarized in Table 2. For this image size, GoG and ToG are  $\sim 1.8$  and  $\sim 1.4$  times slower, respectively, compared with the most computationally efficient focusing criterion tested here (GRA).

In conclusion, we demonstrated a robust and accurate holographic autofocusing criterion that is based on the edge sparsity of the complex wavefront. Analysis showed that it outperforms existing autofocusing approaches for a wide range of objects, at the cost of a modest increase in computation time.

**Funding.** Howard Hughes Medical Institute (HHMI); Army Research Office (ARO); National Science Foundation (NSF); Mary Kay Foundation (TMKF).

## REFERENCES

- U. Schnars and W. Jueptner, *Digital Holography: Digital Hologram Recording, Numerical Reconstruction, and Related Techniques* (Springer, 2010).
- S. Seo, S. O. Isikman, I. Sencan, O. Mudanyali, T.-W. Su, W. Bishara, A. Erlinger, and A. Ozcan, *Anal. Chem.* **82**, 4621 (2010).
- T.-W. Su, L. Xue, and A. Ozcan, *Proc. Natl. Acad. Sci. USA* **109**, 16018 (2012).
- P. Langehanenberg, B. Kemper, D. Dirksen, and G. von Bally, *Appl. Opt.* **47**, D176 (2008).
- A. Greenbaum, Y. Zhang, A. Feizi, P.-L. Chung, W. Luo, S. R. Kandukuri, and A. Ozcan, *Sci. Transl. Med.* **6**, 267ra175 (2014).
- Y. Rivenson, Y. Zhang, H. Gunaydin, D. Teng, and A. Ozcan, "Phase recovery and holographic image reconstruction using deep learning in neural networks," arXiv:1705.04286 (2017).
- F. C. A. Groen, I. T. Young, and G. Ligthart, *Cytometry* **6**, 81 (1985).
- J. Gillespie and R. A. King, *Pattern Recognit. Lett.* **9**, 19 (1989).
- M. Liebling and M. Unser, *J. Opt. Soc. Am. A* **21**, 2424 (2004).
- F. Dubois, C. Schockaert, N. Callens, and C. Yourassowsky, *Opt. Express* **14**, 5895 (2006).
- F. Dubois, A. El Mallahi, J. Dohet-Eraly, and C. Yourassowsky, *Opt. Lett.* **39**, 4286 (2014).
- P. Memmolo, C. Distanto, M. Paturzo, A. Finizio, P. Ferraro, and B. Javidi, *Opt. Lett.* **36**, 1945 (2011).
- P. Memmolo, M. Paturzo, B. Javidi, P. A. Netti, and P. Ferraro, *Opt. Lett.* **39**, 4719 (2014).
- M. Lyu, C. Yuan, D. Li, and G. Situ, *Appl. Opt.* **56**, F152 (2017).
- M. Tamamitsu, Y. Zhang, H. Wang, Y. Wu, and A. Ozcan, "Comparison of Gini index and Tamura coefficient for holographic autofocusing based on the edge sparsity of the complex optical wavefront," arXiv:1708.08055 (2017).
- N. Hurley and S. Rickard, *IEEE Trans. Inf. Theory* **55**, 4723 (2009).
- W. H. Press, S. A. Teukolsky, W. T. Vetterling, and B. P. Flannery, *Numer. Recipes C* **2**, 397 (1992).
- S. Grare, S. Coetmellec, D. Allano, G. Grehan, M. Brunel, and D. Lebrun, *J. Eur. Opt. Soc.* **10**, 15009 (2015).